

Is friction essential for dilatancy and shear jamming in granular matter?

Varghese Babu,^{1,*} Deng Pan,^{2,*} Yuliang Jin,^{2,3,†} Bulbul Chakraborty,⁴ and Srikanth Sastry^{1,‡}

¹*Jawaharlal Nehru Centre for Advanced Scientific Research, Jakkur Campus, Bengaluru 560064, India.*

²*CAS Key Laboratory of Theoretical Physics, Institute of Theoretical Physics,
Chinese Academy of Sciences, Beijing 100190, China*

³*School of Physical Sciences, University of Chinese Academy of Sciences, Beijing 100049, China*

⁴*Martin Fisher School of Physics, Brandeis University, Waltham, MA 02454, USA.*

Granular packings display the remarkable phenomenon of *dilatancy* [1], wherein their volume increases upon shear deformation. Conventional wisdom and previous results suggest that dilatancy, as also the related phenomenon of shear-induced jamming, requires frictional interactions [2, 3]. Here, we investigate the occurrence of dilatancy and shear jamming in frictionless packings. We show that the existence of isotropic jamming densities ϕ_j above the minimal density, the J-point density ϕ_J [4, 5], leads both to the emergence of shear-induced jamming and dilatancy. Packings at ϕ_J form a significant threshold state into which systems evolve in the limit of vanishing pressure under constant pressure shear, irrespective of the initial jamming density ϕ_j . While packings for different ϕ_j display equivalent scaling properties under compression [6], they exhibit striking differences in rheological behaviour under shear. The yield stress under constant volume shear increases discontinuously with density when $\phi_j > \phi_J$, contrary to the continuous behaviour in generic packings that jam at ϕ_J [4, 7].

A large variety of familiar materials, made of macroscopic or mesoscopic constituent particles, may be characterized as *granular matter*. Sands, powders and grains are some examples. Given their large sizes, the individual particles (unlike atoms and molecules in a liquid) do not exhibit spontaneous – *Brownian* – motion, and are thus referred to as being *athermal*. They flow in response to externally applied small forces, but at sufficiently high densities or applied stresses, cease to flow, or *jam* [4, 8]. Density- or stress-driven jamming is of central importance in comprehending a wide variety of complex rheological properties of granular matter, and forms an essential part of a broader understanding of the transition from flowing states of matter to non-flowing or structurally arrested states, including, *e. g.*, the glass transition.

Density-driven jamming, unjamming and yielding of frictionless hard and soft particles have been investigated extensively since the proposal of the jamming phase diagram [4] which has, as originally proposed, a unique density (packing fraction) at ϕ_J characterizing the jamming transition at zero temperature and shear stress. Since then it has been shown that the jamming density ϕ_j is protocol-dependent and therefore not unique [6, 9, 10], satisfying in general $\phi_j \geq \phi_J$ [10]. However, critical behavior associated with jamming, for example the scaling relationship between pressure and density, $p \sim (\phi - \phi_j)$, remains the same, irrespective of ϕ_j [6].

An early proposal that shear deformation, besides density, can induce jamming [8], has recently been explored

extensively in experimental and theoretical investigations, largely of frictional, but also frictionless hard and soft sphere systems [11–22]. In shear jamming, the development of an anisotropic contact network under shear leads to the emergence of a state of finite shear stress and pressure, with their ratio peaking at a density-dependent characteristic strain [11–14, 18–20].

The shear-strain dependent pressure was termed *Reynolds pressure* in [12], reflecting the idea that shear jamming occurs because constant volume conditions frustrate the tendency of granular materials to dilate under shear [1], a phenomenon widely referred to as *dilatancy*. With a similar view, impact-driven and shear-driven jamming in dense suspensions have been related to “frustrated dilatancy” effects [23, 24]. Shear jamming and dilatancy in frictional granular matter have thus been viewed as two sides of the same coin. We clarify that our discussion and investigation concern behaviour under quasistatic shear, and do not always apply when shear rates are finite.

Reynolds’ dilatancy in granular materials has been extensively investigated, motivated by the relevance of the phenomena to soil mechanics [25, 26]. Many available results suggest an intimate relationship between frictional interactions and dilatancy: stress-dilatancy relations couple dilatancy and friction between particles [27]. Recent studies indicate that friction is important for observing shear jamming and dilatancy [28]. Numerical studies [2, 3, 29] have reported, and experiments [24] have also indirectly indicated, the absence of dilatancy in frictionless systems.

These observations are at variance with the simple picture suggested by Reynolds [1], where dilatancy arises purely from geometric exclusion effects of hard parti-

* These authors contributed equally.

† yuliangjin@mail.itp.ac.cn

‡ sastry@jncasr.ac.in

cles, which should therefore be observed also in frictionless systems. We aim here to resolve this paradox, and demonstrate conditions under which dilatancy emerges naturally in frictionless sphere assemblies. We show that such conditions depend critically on the presence of a line of jamming points at densities ϕ_j above ϕ_J .

In motivating our study, we note that, below ϕ_J , initially unjammed frictionless sphere assemblies develop structures under shear, with average geometric contact numbers that increase with density, which can be mechanically stabilized by friction [16]. If the unjammed configurations are at densities above ϕ_J , shear deformations may create contact networks that satisfy the isostatic jamming condition for frictionless packings which are mechanically stable, leading to the possibility of both shear jamming and dilatancy. Thus, the absence of dilatancy [2] and shear jamming [3] in earlier studies could be due to the failure to obtain unjammed initial configurations above ϕ_J rather than to the absence of friction.

We thus investigate assemblies of two models of frictionless spheres prepared to have jamming densities ϕ_j above the minimal jamming density at ϕ_J , explicitly demonstrating the phenomena of shear jamming and dilatancy, and identifying universal features that can be associated to them. Both effects diminish as ϕ_j decreases and vanish as $\phi_j \rightarrow \phi_J$, consistent with previous studies [2, 3, 30].

The two models represent systems that consist of $N = 2000$ (unless otherwise specified) bi-disperse (BD) and poly-disperse (PD) spheres, interacting via a purely-repulsive, harmonic potential $v_{ij}(r) = \frac{1}{2}(1-r/D_{ij})^2$ (zero if $r > D_{ij}$), where r is the inter-particle distance and $D_{ij} = (D_i + D_j)/2$ is the mean diameter (see Methods). Two independent protocols are used to create initially unjammed states whose jamming densities ϕ_j are above ϕ_J (see Methods for details). (i) Mechanical annealing of the BD system by the application of cyclic athermal quasistatic shear (AQS) results in unjamming of packings in the density range above $\phi_J \simeq 0.648$, as described in [31]. These unjammed configurations correspond to packings with jamming densities $\phi_j \in [0.648, 0.661]$. (ii) Thermal annealing of the PD system, with the help of an extremely efficient Monte Carlo algorithm which involves artificial swap dynamics [32], is used to generate configurations with jamming densities $\phi_j \in [0.655, 0.69]$, above $\phi_J \simeq 0.655$.

We first show that, an unjammed configuration at $\phi < \phi_j$, where $\phi_j > \phi_J$, can be jammed at a certain strain γ_j by uniform constant volume AQS. The onset of shear jamming is characterised consistently by a steep increase of the shear stress σ_{xz} (Fig. 1(a) and (b)), of the non-rattler contact number Z_{NR} (Fig. 1(c)), of the pressure (Fig. S1(a) and (b) and Fig. S2 of Supplementary Information (SI)), and of the potential energy PE (Fig. S1(c) and (d)), around γ_j . We observe that Z_{NR} exceeds the isostatic value $Z_{iso} = 2D = 6$, where $D = 3$ is the spatial dimensionality, for $\gamma > \gamma_j$, indicating that the shear jammed systems are mechanically stable. The non-

rattler contact number Z_{NR} jumps discontinuously at γ_j (Fig. 1(c)), associated with an abrupt increase of the potential energy PE (Fig. 1(d)). The value of γ_j , as well as the stress overshoot amplitude, depends on the distance to the isotropic jamming $\delta\phi = \phi_j - \phi$, and the value of ϕ_j that characterizes the degree of mechanical/thermal annealing in the initial preparation procedure (Fig. 1 (b)). The data of $PE(Z_{NR})$, on the other hand, follow a universal function on the jamming side $Z_{NR} > Z_{iso}$, that is independent of the jamming strain γ_j , the model, and the jamming protocol (shear or compression), see (Fig. 1(d)). The data for $\phi_j \approx \phi_J$ in Fig. 1 (b) also clearly show that shear jamming disappears in the limit $\phi_j \rightarrow \phi_J$.

We next show that packings with $\phi_j > \phi_J$ dilate under constant pressure AQS. For this purpose, we modify the original AQS protocol, which is based on energy minimization at constant volume, to minimize instead the enthalpy, allowing changes in the volume of the simulation box to ensure a fixed pressure (see Methods). In this constant pressure AQS protocol, the system traverses only those potential energy minima that have the specified pressure, P . Since the pressure is finite, the system is jammed throughout this process. For both BD and PD models, during the constant pressure shear deformation the system dilates until reaching a *steady-state* at packing fraction ϕ_s which depends on the pressure applied (Fig. 2). Correspondingly, the stress σ_{xz} increases initially with strain, and eventually also reaches a steady-state plateau after an overshoot (Fig. 2(b) and 2(d)). The magnitude of stress overshoot is more significant in systems with larger ϕ_j . The presence of a maximum at a characteristic value of the strain is the constant pressure analog of the maximum in stress anisotropy observed in the constant volume protocol as shown in the SI Fig. S3 (a) and (b). The development of the maximum in the stress anisotropy, or in the macroscopic friction $\mu = \sigma_{xz}/P$, therefore, seems to be a universal feature associated with shear jamming and dilatancy, in both frictionless [15] and frictional systems, under both uniform [14, 22, 33, 34] and cyclic shear deformations [20].

The amount of dilation, $\delta\phi = \phi_{init} - \phi_s$, where ϕ_{init} is the initial density, increases with ϕ_j and decreases with P , as seen from Fig. 2(a) and 2(c) and shown in Fig. S4 of the SI. In the limit $\phi_j \rightarrow \phi_J$ and $P \rightarrow 0$, the dilation effect disappears ($\delta\phi \rightarrow 0$), which is consistent with previous results [2]. The PD model shows more significant dilation, because higher ϕ_j , relative to ϕ_J , is obtained, thanks to the efficient swap algorithm.

Steady-states, which are reached at sufficiently large strains under both constant pressure and constant volume shear deformations, are memoryless: they follow equations of states (EOSs), $P_s(\phi_s)$ and $\sigma_{xz,s}(\phi_s)$, which are independent of initial conditions (ϕ_j), as shown in Fig. 3(a) and 3(b). Extrapolating the EOSs to the limit of zero pressure and stress, we find that the steady-states converge to a *critical state* at density ϕ_c , i.e., $P_s(\phi_s \rightarrow \phi_c) \rightarrow 0$ and $\sigma_{xz,s}(\phi_s \rightarrow \phi_c) \rightarrow 0$, where $\phi_c \approx 0.648$ for the BD and $\phi_c \approx 0.656$ for the PD models

(Fig. 3(c)). Within our numerical precision, the critical-state density ϕ_c coincides with the J-point density ϕ_J in large systems (see Fig. S5 in SI for finite-size analysis), $\phi_c \simeq \phi_J$, which confirms the absence of dilatancy in the limit $\phi_j \rightarrow \phi_J$.

Despite the fact that the steady-state stress is anisotropic, $P_s(\phi_s)$ agrees well with the isotropic EOS, $P_{iso}(\phi)$, obtained by an isotropic compression from ϕ_J (Fig. 3(a)). The critical scaling of P_s also obeys a linear relationship, $P_s(\phi_s) \sim \phi_s - \phi_c$, as in the isotropic jamming case, where $P_{iso} \sim \phi - \phi_J$ [5]. Fig. 3(a) further shows that, up a scale factor, the EOSs for pressure collapse onto the same master curve, that is not only independent of the initial condition (ϕ_j), but also the polydispersity (BD or PD model), and the jamming protocol (constant volume shear, constant pressure shear, or isotropic compression). The stress EOS $\sigma_{xz,s}(\phi_s)$ of steady-states (Fig.3(b)) for the different shear protocols collapses on to a master curve, but unlike pressure, we cannot compare with the isotropic compression case, where the shear stress is always zero. Fig. 3 (c) shows the steady-state packing fraction ϕ_s vs. pressure, indicating more clearly the approach to the asymptotic density as pressure goes to zero, independently of protocol, but different for the two studied systems. Figure 3 (d) shows that, the macroscopic friction of steady states $\mu_s = \sigma_{xz,s}/P_s$ is non-zero, and slowly decreases with pressure as $\mu_s = \mu_0 - cP_s^\beta$, where $\mu_0 = 0.113, \beta = 0.453$ for the BD model, and $\mu_0 = 0.122, \beta = 0.458$ for the PD model, which are model-independent within the numerical error. The values of μ_0 are also close to the previously reported data $\mu_0 \simeq 0.1$ for mono-disperse spheres with Hertzian interactions [2]. This scaling of μ_s suggests that, near the critical-state ($\phi_s \rightarrow \phi_c$), the stress is proportional to the pressure, $\sigma_{xz,s} \sim \mu_0 P_s$, and the stress EOS is linear, $\sigma_{xz,s}(\phi_s) \sim \phi_s - \phi_c$, as confirmed in SI S9 Fig (b). Further details may be found in the SI, Fig.s S6 - S9.

To summarize the above described behaviors on shear jamming and dilatancy, we propose a generalized zero-temperature jamming phase diagram. The original jamming phase diagram, introduced by Liu and Nagel [4], conjectures that, in the athermal limit, the jammed states at ϕ_J should be extremely fragile under shear – the yield stress vanishes at ϕ_J continuously from above jamming, $\sigma_Y(\phi_J) = 0$, suggesting that infinitesimal shear stress is required to yield (unjam) a packing at ϕ_J . While this picture is well supported by previous numerical studies where $\phi_j \approx \phi_J$ [2, 5, 7], here we show explicitly a remarkable discontinuity of the yield stress σ_Y (as well as the yield pressure P_Y) at the jamming density ϕ_j , when $\phi_j > \phi_J$ (Fig. 4 for the PD system; See SI Fig. S10 for BD). This discontinuous nature is independent of the definition of σ_Y (here we define $\sigma_Y = \sigma_s$, see SI Fig.S11 for other definitions).

On the contrary, the pressure P_{iso} under isotropic compression vanishes continuously at ϕ_j (Fig. 4(a)), which is independent of ϕ_j , as shown previously [6]. It demon-

strates the reason why under constant pressure shear, the volume expands from the initial isotropic states to the final steady-states (Fig. 2), and under constant volume shear, the pressure increases (SI Fig. S1 a) and b)), see Fig. 4(a). The unjammed states below ϕ_j jam under constant volume shear, as shown in Fig. 1. Interestingly, the yield stress σ_Y of shear jammed systems at a constant density ϕ below ϕ_j appear to be a continuation of that of isotropically jammed ones. This observation is consistent with the universality of the EOSs as shown in Fig. 3. We therefore generalize the zero-temperature jamming phase diagram for frictionless spheres to arbitrary ϕ_j , as shown schematically in Fig. 4, where the stress jump $\sigma_Y(\phi_j)$ at the isotropic jamming transition point ϕ_j vanishes as $\phi_j \rightarrow \phi_J$, as does the regime of shear jamming.

We conclude by firstly comparing the dilatancy effect between amorphous and lattice assemblies. In the original paper [1] where the concept of “dilatancy” was introduced for the first time, Reynolds proposed a pure geometric mechanism based on the idea that one type of lattice packing (e.g., face-centered cubic) could expand its volume under shear by transforming into another type of lattice packing (e.g., body-centered cubic). Here we recover the same geometric mechanism for amorphous packings, which has been missed in previous studies [2, 29]. Like lattices, the amorphous ensemble also includes multiple states with different packing densities, although jammed packings at densities above ϕ_J are exponentially more abundant [9]. The paths connecting these states, driven by external agitations such as shear, are accompanied by dilatancy, shear jamming, and additional rich phenomena such as avalanches, plasticity, shear softening and hardening, and yielding. Although generic protocols lead to jammed systems with $\phi_j \sim \phi_J$, where friction is necessary for dilatancy [24, 35], here we propose a novel approach based on cyclic shear, which can be reproduced in experiments to generate packings with $\phi_j > \phi_J$. Our research therefore opens the way for experimental studies on exploring the complex phase space of jamming.

METHODS

Models

(i) Bi-disperse model. The bi-disperse system consists of N equal-mass spheres with a diameter ratio $D_1/D_2 = 1.4$ and a number ratio $N_1/N_2 = 1$.

(ii) Poly-disperse model. The PD system contains N equal-mass spheres whose diameter distribution is characterized by $P(D) \sim D^{-3}$, for $D_{\min} \leq D \leq D_{\min}/0.45$. The volume fraction is $\phi = \rho(1/6)\pi\bar{D}^3$, where ρ is the number density N/V , and V is the volume of simulation box.

Constant volume athermal quasi-static shear

(i) In the BD model, constant volume AQS simulations are carried out using LAMMPS[36]. To simulate a uniform simple shear deformation, at each step an affine

transformation is applied to the position of each particle, $x' = x + \delta\gamma \times z, y' = y, z' = z$, where $\delta\gamma = 10^{-4}$, followed by energy minimization using the conjugate gradient (CG) method. The CG procedure stops when the maximum component of the force vector is less than 10^{-16} . The energy minimization stops when the maximum distance moved by any particle is less than the machine precision during an iteration. The norm of the equilibrium net force vector is of the order of 10^{-13} and the maximum component is of the order of 10^{-14} at the termination of minimization.

(ii) In the PD model, the affine transformation is applied with step size $\delta\gamma = 10^{-4}$, followed by energy minimization using the FIRE algorithm [37]. The minimization procedure stops when the fraction of force balanced particles with net force magnitude $|f| \leq 10^{-14}$ grows above 0.995.

Constant pressure athermal quasi-static shear

In constant pressure AQS simulations, the energy minimization is replaced by the minimization of enthalpy $H = U + PV$ at the imposed pressure P . (i) In the BD model, the minimization stops when the maximum distance moved by any particle during a minimization step is less than the machine precision. (ii) In the PD model, the minimization stops if the fraction of force balanced particles is greater than 0.995, and the deviation from the target pressure is less than 10^{-4} .

Protocols to prepare initial configurations

(i) Mechanical annealing by cyclic athermal quasistatic shear for the BD model. We first use the method in [6] to generate packings with jamming density $\phi_J \approx 0.648$. The initial configurations are hard-sphere configurations at a packing fraction of $\phi = 0.363$, which are equilibrated using the Monte-Carlo (MC) algorithm. We switch to the harmonic soft-sphere potential, rapidly compress the configurations by rescaling the volume of the simulation box (till $\beta P/\rho$ decays to ~ 1000 , where β is the inverse temperature), and remove the resulting overlaps by using MC simulations. The temperature is then switched off, and the system is further quasi-statically compressed, by inflating the particles uniformly, followed by energy minimization using the conjugate gradient method. The compression stops when the energy per particle $e = E/N$, after minimization, remains above 10^{-16} . This is used as the criterion for jamming. Then the system is slowly decompressed till $e < 10^{-16}$, which generates configurations corresponding to jamming density $\phi_J \approx 0.648$.

We then use mechanical annealing to increase the jamming density from ϕ_J to $\phi_j > \phi_J$. The configurations obtained from the above procedure are compressed to various over-jamming densities $\phi > \phi_J$, and are unjammed using cyclic AQS, $\gamma = 0 \rightarrow \gamma_{max} \rightarrow 0 \rightarrow -\gamma_{max} \rightarrow 0$, where the strain amplitude $\gamma_{max} = 0.07$ [31], and the strain step $\delta\gamma = 10^{-3}$. These configurations correspond to jamming densities $\phi_j > \phi_J$. See SI Fig. S12 for the dependence of ϕ_j on protocol parameters.

(ii) Thermal annealing by a swap algorithm for the PD model. We first prepare dense equilibrium HS configurations at ϕ_g , using the swap algorithm [32]. At each swap MC step, we exchange the positions of two randomly picked particles as long as they do not overlap with other particles. Combined with standard event-driven molecular dynamics (MD), such non-local swap moves significantly speed up the equilibration procedure. The poly-dispersity of the model suppresses crystallization even in deep annealing, and optimizes the efficiency of the algorithm [32].

For each equilibrium configuration at ϕ_g , we then perform a rapid quench to generate the jammed configuration at ϕ_j (see Ref. [38] for the relationship between ϕ_g and ϕ_j). In particular, the J-point state at $\phi_J \simeq 0.655$ are quenched from random initial configurations with $\phi_g = 0$ [5]. The rapid quench is realized by inflating the particle sizes instantaneously to reach the target density, switching to the harmonic soft-sphere potential, and then minimizing the total potential energy using the FIRE algorithm [37]. The same jamming criterion is used as in the BD model.

Calculation of the stress tensor and the pressure

The stress tensor is calculated using the formula,

$$\hat{\sigma} = -\frac{1}{V} \sum_{i < j} \vec{f}_{ij} \otimes \vec{r}_{ij}, \quad (1)$$

where \vec{f}_{ij} and \vec{r}_{ij} are the inter-particle force and distance vectors between particles i and j . The pressure P is related to the trace of the stress tensor, $P = -(\sigma_{xx} + \sigma_{yy} + \sigma_{zz})/3$, which can be written as,

$$P = \frac{1}{3V} \sum_{i < j} \vec{f}_{ij} \cdot \vec{r}_{ij}. \quad (2)$$

-
- [1] Osborne Reynolds. Lvii. on the dilatancy of media composed of rigid particles in contact. with experimental illustrations. *The London, Edinburgh, and Dublin Philosophical Magazine and Journal of Science*, 20(127):469–481, 1885.
- [2] Pierre-Emmanuel Peyneau and Jean-Noël Roux. Frictionless bead packs have macroscopic friction, but no dilatancy. *Physical review E*, 78(1):011307, 2008.
- [3] Marco Baity-Jesí, Carl P Goodrich, Andrea J Liu, Sid-

- ney R Nagel, and James P Sethna. Emergent so(3) symmetry of the frictionless shear jamming transition. *Journal of Statistical Physics*, 167(3-4):735–748, 2017.
- [4] Andrea J Liu and Sidney R Nagel. Nonlinear dynamics: Jamming is not just cool any more. *Nature*, 396(6706):21, 1998.
- [5] Corey S O’hern, Leonardo E Silbert, Andrea J Liu, and Sidney R Nagel. Jamming at zero temperature and zero applied stress: The epitome of disorder. *Physical Review*

- E, 68(1):011306, 2003.
- [6] Pinaki Chaudhuri, Ludovic Berthier, and Srikanth Sastry. Jamming transitions in amorphous packings of frictionless spheres occur over a continuous range of volume fractions. *Physical review letters*, 104(16):165701, 2010.
 - [7] Claus Heussinger and Jean-Louis Barrat. Jamming transition as probed by quasistatic shear flow. *Physical review letters*, 102(21):218303, 2009.
 - [8] M E Cates, J P Wittmer, J.-P. Bouchaud, and P Claudin. Jamming, force chains, and fragile matter. *Phys. Rev. Lett.*, 81:1841–1844, 1998.
 - [9] Giorgio Parisi and Francesco Zamponi. Mean-field theory of hard sphere glasses and jamming. *Reviews of Modern Physics*, 82(1):789, 2010.
 - [10] Misaki Ozawa, Takeshi Kuroiwa, Atsushi Ikeda, and Kunimasa Miyazaki. Jamming transition and inherent structures of hard spheres and disks. *Physical review letters*, 109(20):205701, 2012.
 - [11] Dapeng Bi, Jie Zhang, Bulbul Chakraborty, and Robert P Behringer. Jamming by shear. *Nature*, 480(7377):355, 2011.
 - [12] Jie Ren, Joshua A Dijkstra, and Robert P Behringer. Reynolds pressure and relaxation in a sheared granular system. *Physical review letters*, 110(1):018302, 2013.
 - [13] Sumantra Sarkar, Dapeng Bi, Jie Zhang, RP Behringer, and Bulbul Chakraborty. Origin of rigidity in dry granular solids. *Phys. Rev. Lett.*, 111(6):068301, 2013.
 - [14] S. Sarkar, D. Bi, J. Zhang, J. Ren, R.P. Behringer, and B. Chakraborty. Shear-induced rigidity of frictional particles: Analysis of emergent order in stress space. *Physical Review E*, 93(4), 2016.
 - [15] Nishant Kumar and Stefan Luding. Memory of jamming–multiscale models for soft and granular matter. *Granular Matter*, 18(3):58, 2016.
 - [16] HA Vinutha and Srikanth Sastry. Disentangling the role of structure and friction in shear jamming. *Nature Physics*, 12(6):578, 2016.
 - [17] H A Vinutha, Kabir Ramola, Bulbul Chakraborty, and Srikanth Sastry. Timescale divergence at the shear jamming transition. *arXiv preprint arXiv:1903.01496*, 2019.
 - [18] Ryohei Seto, Abhinendra Singh, Bulbul Chakraborty, Morton M Denn, and Jeffrey F Morris. Shear jamming and fragility in dense suspensions.
 - [19] Michio Otsuki and Hisao Hayakawa. Discontinuous change of shear modulus for frictional jammed granular materials. *Physical Review E*, 95(6):1–10, 2017.
 - [20] Michio Otsuki and Hisao Hayakawa. Shear jamming, discontinuous shear thickening, and fragile states in dry granular materials under oscillatory shear. *Physical Review E*, 101(3):032905, 2020.
 - [21] Yuliang Jin, Pierfrancesco Urbani, Francesco Zamponi, and Hajime Yoshino. A stability-reversibility map unifies elasticity, plasticity, yielding, and jamming in hard sphere glasses. *Science Advances*, 4(12), 2018.
 - [22] Yiqiu Zhao, Jonathan Barés, Hu Zheng, Joshua E. S. Socolar, and Robert P. Behringer. Shear-Jammed, Fragile, and Steady States in Homogeneously Strained Granular Materials. *Physical Review Letters*, 123(15):1–7, 2019.
 - [23] E. Brown and H. M. Jaeger. The role of dilation and confining stresses in shear thickening of dense suspensions. *J. Rheol.*, 56:875–923, 2012.
 - [24] Cécile Clavaud, Antoine Bérut, Bloen Metzger, and Yoël Forterre. Revealing the frictional transition in shear-thickening suspensions. *Proc. Natl. Acad. Sci. U.S.A.*, pages 5147–5152, 2017.
 - [25] Nicolaas P Kruijdt and L Rothenburg. A micromechanical study of dilatancy of granular materials. *Journal of the Mechanics and Physics of Solids*, 95:411–427, 2016.
 - [26] K Kesava Rao and Prabhu R Nott. *An introduction to granular flow*/K. Kesava Rao, Prabhu R. Nott. 2008.
 - [27] Peter W Rowe. The stress-dilatancy relation for static equilibrium of an assembly of particles in contact. *Proceedings of the Royal Society of London. Series A. Mathematical and Physical Sciences*, 269(1339):500–527, 1962.
 - [28] Robert P Behringer and Bulbul Chakraborty. The physics of jamming for granular materials: a review. *Reports on Progress in Physics*, 82(1):012601, 2018.
 - [29] Émilien Azéma, Farhang Radjaï, and Jean-Noël Roux. Internal friction and absence of dilatancy of packings of frictionless polygons. *Physical Review E*, 91(1):010202, 2015.
 - [30] Thibault Bertrand, Robert P Behringer, Bulbul Chakraborty, Corey S O’Hern, and Mark D Shattuck. Protocol dependence of the jamming transition. *Physical Review E*, 93(1):012901, 2016.
 - [31] Pallabi Das, H A Vinutha, and Srikanth Sastry. Unified phase diagram of reversible-irreversible, jamming and yielding transitions in cyclically sheared soft sphere packings. *arXiv preprint arXiv:1907.08503*, 2019.
 - [32] Ludovic Berthier, Daniele Coslovich, Andrea Ninarello, and Misaki Ozawa. Equilibrium sampling of hard spheres up to the jamming density and beyond. *Phys. Rev. Lett.*, 116:238002, Jun 2016.
 - [33] Sumantra Sarkar, Elan Shatoff, Kabir Ramola, Romain Mari, Jeffrey Morris, and Bulbul Chakraborty. Shear-induced organization of forces in dense suspensions: signatures of discontinuous shear thickening. In *EPJ Web of Conferences*, volume 140, page 09045. EDP Sciences, 2017.
 - [34] R. Seto, A. Singh, B. Chakraborty, M. M Denn, and J. F Morris. Shear jamming and fragility in dense suspensions. *arXiv preprint arXiv:1902.04361*, 2019.
 - [35] A. Singh, R. Mari, M. M. Denn, and J. F. Morris. A constitutive model for simple shear of dense frictional suspensions. *J. Rheol.*, 62(2):457–468, 2018.
 - [36] Steve Plimpton. Fast parallel algorithms for short-range molecular dynamics. *Journal of computational physics*, 117(1):1–19, 1995.
 - [37] Erik Bitzek, Pekka Koskinen, Franz Gähler, Michael Moseler, and Peter Gumbsch. Structural relaxation made simple. *Physical review letters*, 97(17):170201, 2006.
 - [38] Ludovic Berthier, Patrick Charbonneau, Yuliang Jin, Giorgio Parisi, Beatriz Seoane, and Francesco Zamponi. Growing timescales and lengthscales characterizing vibrations of amorphous solids. *Proceedings of the National Academy of Sciences*, 113(30):8397–8401, 2016.
 - [39] Daniele Coslovich, Ludovic Berthier, and Misaki Ozawa. Exploring the jamming transition over a wide range of critical densities. *SciPost Physics*, 3(4):027, 2017.
 - [40] Claus Heussinger, Pinaki Chaudhuri, and Jean-Louis Barrat. Fluctuations and correlations during the shear flow of elastic particles near the jamming transition. *Soft matter*, 6(13):3050–3058, 2010.
 - [41] Wen Zheng, Shiyun Zhang, and Ning Xu. Jamming of packings of frictionless particles with and without shear. *Chinese Physics B*, 27(6):066102, 2018.

- [42] Daniel Vågberg, Peter Olsson, and Stephen Teitel. Glassiness, rigidity, and jamming of frictionless soft core disks. Physical Review E, 83(3):031307, 2011.

ACKNOWLEDGMENTS

We warmly thank K. Miyazaki, T. Kawasaki, M. Otsuki, for discussions. Y.J. acknowledges funding from Project 11974361, Project 11935002, and Project 11947302 supported by NSFC, from Key Research Program of Frontier Sciences, CAS, Grant NO. ZDBS-LY-7017, and from the CAS Pioneer Hundred Talents Program. BC acknowledges support from NSF-CBET-1916877, BSF-2016188. and a Simons Fellowship in Theoretical Physics. SS acknowledges support through the J. C. Bose Fellowship, SERB, DST, India. BC and SS acknowledge the support of the Indo-US Virtual Networked Joint Center project titled Emergence and Remodeling of force chains in soft and Biological Matter No. IUSSTF/JC-026/2016. The computations were performed using resources at TUS-CMS, JNCASR, the HPC Cluster of ITP-CAS, Tianhe-2 Supercomputer and National Supercomputer Center in Guangzhou.

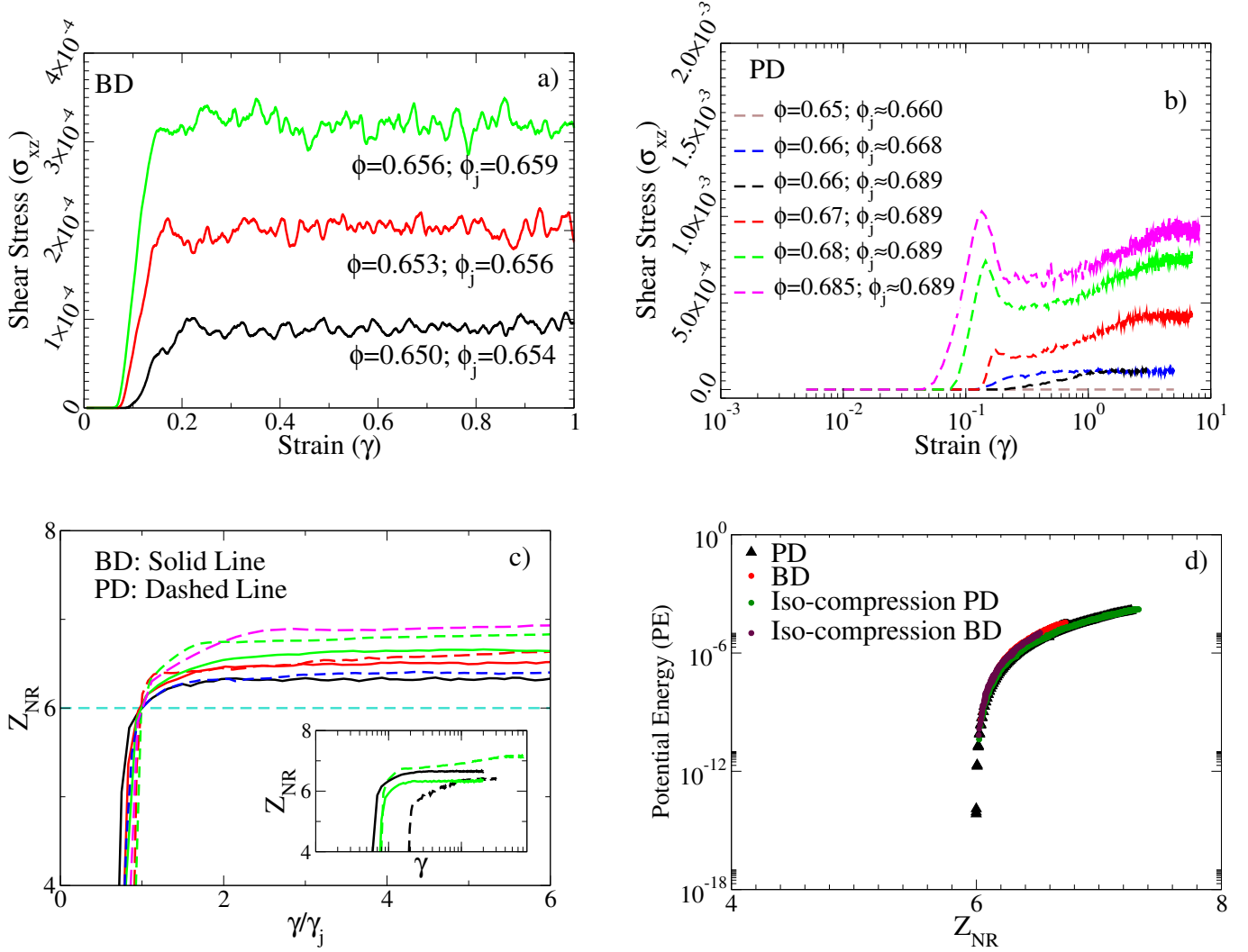


FIG. 1. **Shear jamming.** Shear stress σ_{xz} as a function of strain γ for (a) BD model, (b) PD model, and a few different ϕ_j and ϕ . (c) Non-rattler contact number Z_{NR} , which is calculated after removing rattlers (particles with less than $D+1$ contacts) recursively, as a function of γ/γ_j . Inset shows unscaled data, configurations at different densities jam at different strains. (d) The potential energy PE is a universal function of Z_{NR} above jamming, for both BD and PD systems, for different ϕ_j and ϕ (and therefore different γ_j), and for both compression and shear jamming. The data are averaged over 20 and 64 independent samples in BD and PD systems respectively.

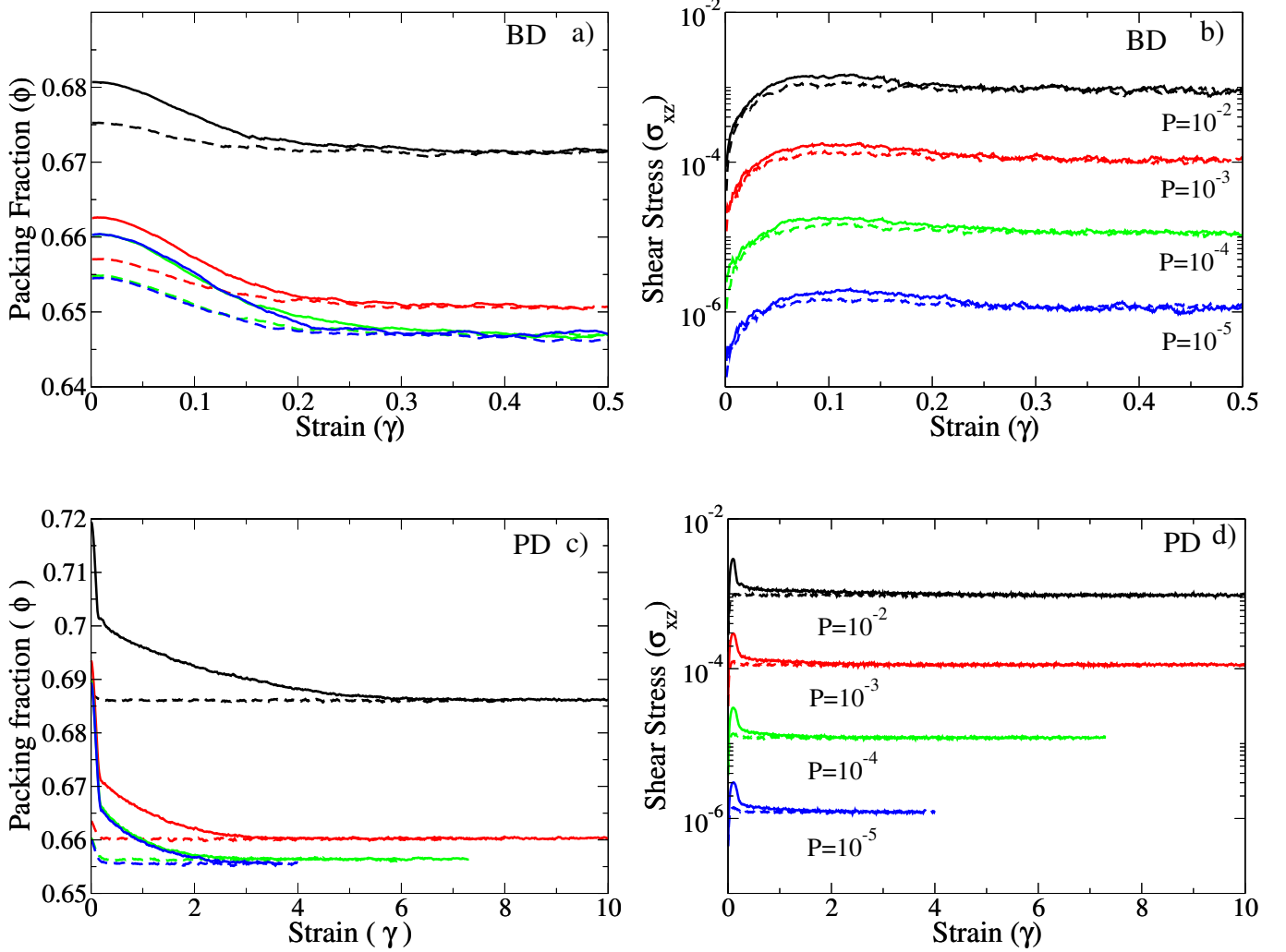


FIG. 2. **Dilatancy.** The evolution of (a) packing fraction ϕ and (b) shear stress σ_{xz} as functions of strain γ under constant pressure AQS in the BD model, for $\phi_j = 0.654$ (dashed) and $\phi_j = 0.66$ (solid), and for a few different pressures P (indicated in (b)). (c,d) Same data in the PD model (P values indicated in (d)), for $\phi_j = 0.660$ (dashed) and $\phi_j = 0.689$ (solid). The data are averaged over 10 and 64 independent samples in BD and PD systems respectively.

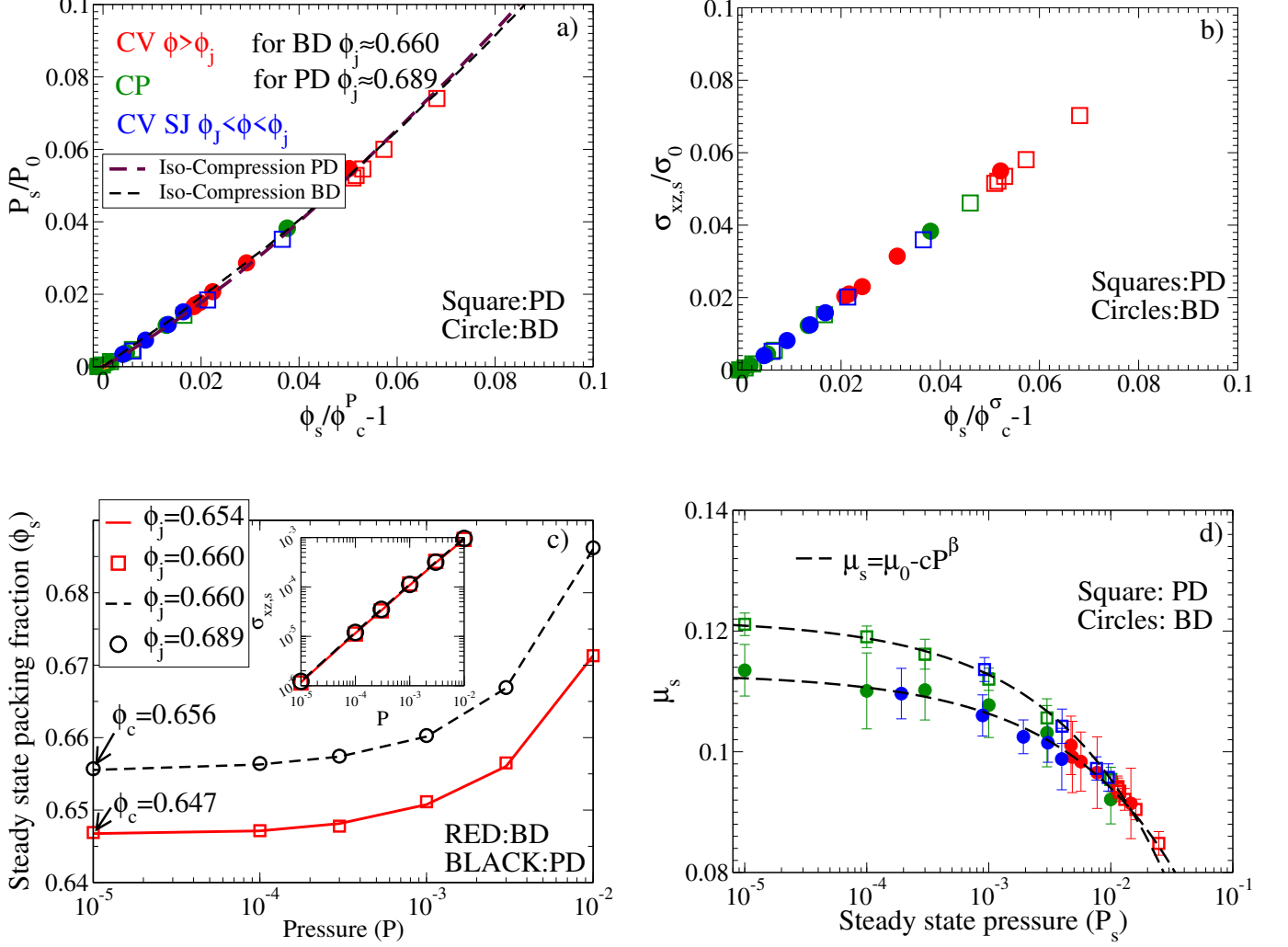


FIG. 3. **Steady-state EOSs.** (a) The steady-state pressure P_s is a universal function of $\phi_s/\phi_c^P - 1$ after rescaling, where for the BD model, the scaling factor $P_0 = 0.261$ and the jamming density $\phi_j = 0.66$, and for the PD model, $P_0 = 0.217$ and $\phi_j = 0.689$. The data are obtained from constant volume shear above ϕ_j (red), constant volume shear below ϕ_j where shear jamming occurs (blue), constant pressure shear (green), and isotropic compression from ϕ_j where P_{iso} is plotted as a function of $\phi/\phi_j - 1$ with $P'_0 = 0.21$ for PD and $P'_0 = 0.29$ for BD. (b) Steady-state stress $\sigma_{xz,s}$ is a universal function of $\phi_s/\phi_c^\sigma - 1$. The rescaling factor $\sigma_0 = 0.024$ for BD and $\sigma_0 = 0.021$ for PD. (c) Steady-state density ϕ_s as a function of pressure P_s for different ϕ_j , obtained from constant pressure shear. Inset: Steady-state stress is independent of the jamming density for constant pressure shear deformation. (d) Macroscopic friction μ_s of steady-states as a function of pressure P_s .

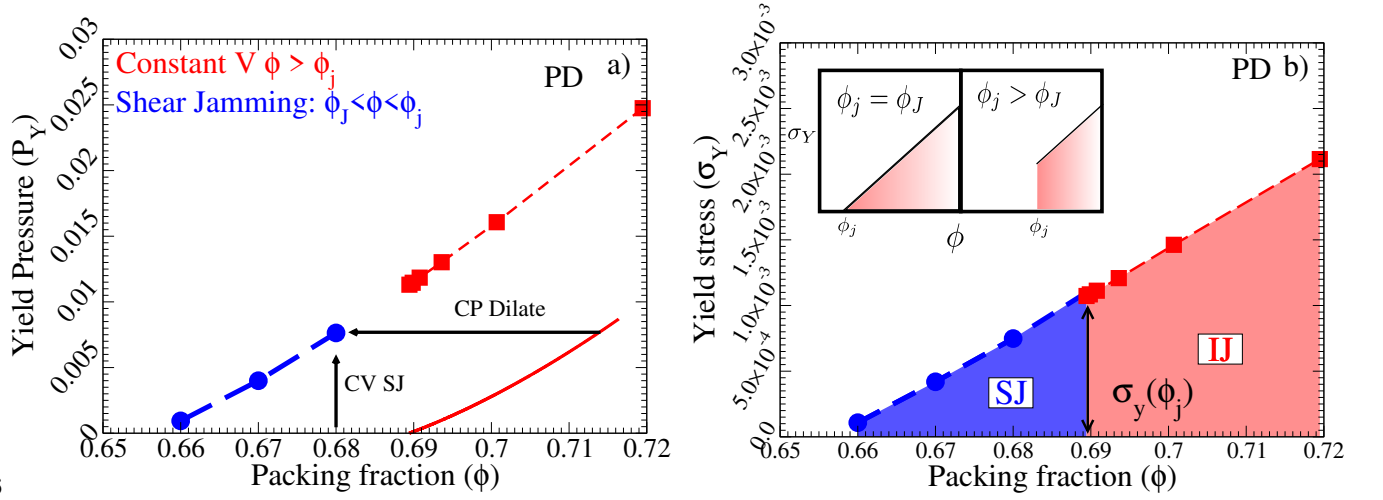


FIG. 4. **Generalized zero-temperature jamming phase diagram.** a) Yield pressure P_Y (where $P_Y = P_s$) and b) yield stress σ_Y (where $\sigma_Y = \sigma_s$) as functions of volume fraction ϕ , obtained from constant volume shear of PD systems above $\phi_j = 0.689$ (red points) and below (blue points). (see SI Fig. S10 for similar plots for the BD model). Above ϕ_j , the system is initially jammed by the isotropic compression (IJ), and remains jammed under shear as long as $\sigma_{xz} < \sigma_Y$, while below ϕ_j , the initially unjammed system is shear jammed (SJ) at γ_j (Fig. 1), and becomes unjammed again (yields) once σ_{xz} reaches σ_Y . The isotropic compression EOS $P_{iso}(\phi)$ is also plotted (red line). The same data are shown in Fig. 3(a) and (b) in rescaled plots.

Appendix A: Is friction essential for dilatancy and shear jamming in granular matter? (Supplementary Information)

1. Additional data for shear jamming

The unjammed configurations at a density ϕ , where $\phi_J < \phi < \phi_j$, undergo shear jamming when subjected to steady shear at constant volume. Shear jamming can be detected by a sharp increase in the stress σ_{xz} and in the coordination number Z_{NR} with increasing strain, as shown in Fig. 1. Additionally, FIG S1 shows how the pressure P and the potential energy PE increase with strain. In the mechanical annealing protocol, the shear jamming strain γ_j , which is indicated by an abrupt jump of the pressure P in FIG S2, is always greater than $\gamma_{max} = 0.07$, the training amplitude used in the cyclic shearing.

We also calculate the macroscopic friction $\mu = \sigma_{xz}/P$ of the configurations as a function of $\gamma - \gamma_j$ (FIG S3), which shows a peak in the cases when there is a significant overshoot in the stress-strain curve (Fig. 1). This peak, appearing after the shear jamming strain γ_j , also exists in the uniform shear of over-compressed systems (FIG S8). In both cases, the peak occurs near the yielding point.

2. Additional data for the dilatancy effect under constant pressure shear

Figure S4 shows that, under constant pressure shear deformations, the amount of dilation $\delta\phi = \phi_{init} - \phi_s$, which is the difference between the initial density ϕ_{init} and the steady-state density ϕ_s , increases with the jamming density ϕ_j for a fixed pressure P , or decreases with P for a fixed ϕ_j .

3. Finite Size analysis of the J-point density ϕ_J and the steady-state density ϕ_c

We perform a finite size analysis of both the J-point density ϕ_J and the steady-state density ϕ_c for the PD model. Our analysis is based on simulation data obtained from systems that consist of $N = 250, 500, 1000, 2000, 4000$ particles, with 256, 192, 128, 64, 64, 64 independent samples respectively.

To estimate the J-point density ϕ_J , we follow the procedure employed in Ref [39]: starting from a random initial configuration, the system is compressed and decompressed iteratively, followed with energy minimization after each step, until reaching the jamming/unjamming threshold where the energy is infinitesimally positive. More specifically, the particles are inflated instantly to increase the volume fraction by $\delta\phi = 5 \times 10^{-4}$ during each compression step. After that, we minimize the energy of the system using the FIRE algorithm [36]. If the system is jammed (the residual potential energy per particle after minimization is larger than 10^{-16}), we decrease $\delta\phi$ by a factor of 2 and decompress the system until it becomes unjammed. We perform a series of decompression and compression as described above, until $\delta\phi < 10^{-6}$. Lastly, we perform an additional cycle of compression and decompression: the compression is performed with $\delta\phi = 10^{-5}$ until the residual energy per particle is larger than 10^{-6} , and the decompression is performed with $\delta\phi = 10^{-6}$ until the jammed system becomes unjammed. We identify this unjamming density as ϕ_J .

To estimate the steady-state density ϕ_c , we perform constant pressure AQS at a few different P_s , by minimizing the enthalpy using the FIRE algorithm, and measure the volume fraction $\phi_s(P_s)$ when the stress reaches a constant value. Then we extrapolate ϕ_c from $\phi_s(P_s)$ using the linear relation $\phi_s - \phi_c \sim P_s$ near the zero pressure limit.

The system size dependences of ϕ_J and ϕ_c are shown in FIG. S5 a), and the difference $\phi_c - \phi_J$ is plotted as a function of the system size N in FIG. S5 b). Our results show that ϕ_c is always slightly larger than ϕ_J in finite size systems, but the difference decreases with N . In this paper, we regard $\phi_J \simeq \phi_c$ in the thermodynamical limit $N \rightarrow \infty$. However, note that several previous studies [40–42] in two dimensions suggested that this difference remains finite (around 0.001-0.002), even in the

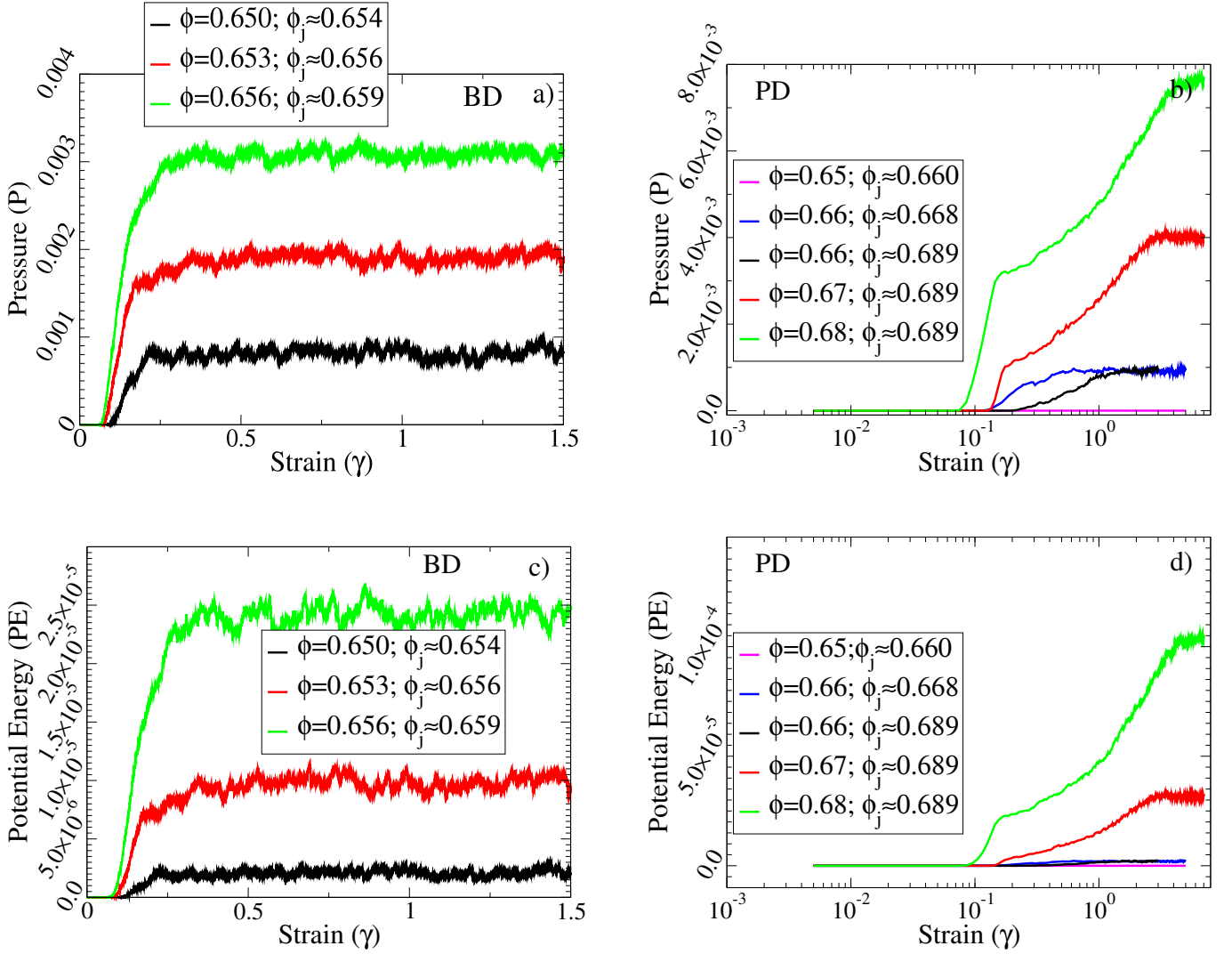


FIG. S1. **Evolutions of (a-b) pressure P and (c-d) potential energy PE with strain γ during shear jamming.** The constant volume uniform athermal quasi-static shear (AQS) is applied. Data are presented for a few different ϕ and ϕ_j , obtained in both bi-disperse (BD) and poly-disperse (PD) systems.

thermodynamical limit. We do not exclude such a possibility in three dimensions based on our data.

4. Dilatancy effect revealed by pressure increase under constant volume shear

For over-compressed systems with a jamming density ϕ_j above ϕ_J , the pressure P increases under constant volume shear deformations, which is an effect equivalent to dilatancy in constant pressure shear. FIG S6 shows how the pressure P increases from P_{init} when the constant volume shear is applied, and FIG S8 shows the evolutions of the macroscopic friction μ . We find that the peak in macroscopic friction is more prominent for configurations with a larger ϕ_j . The scaling relationship between

the steady-state macroscopic friction μ_s and pressure P_s , $\mu_s = \mu_0 - cP_s^\beta$, is shown in FIG S7. Note that, in Fig. 1 of the main text and Sec. A 1, the initial configurations are unjammed ($P_{init} = 0$ or $\phi < \phi_j$). In that case, the constant volume shear deformation firstly jams the system, and then increases the pressure (see FIG S1).

5. Additional data for equations of state

a. Equations of state of steady-states

Here we explain how to obtain the steady-state equations of state (EOSs) of pressure $P_s(\phi_s)$ and of stress $\sigma_{xz,s}(\phi_s)$. For the EOS of pressure, we firstly calculate the average pressure-strain curve $P(\gamma) = \langle P^{ind}(\gamma) \rangle$

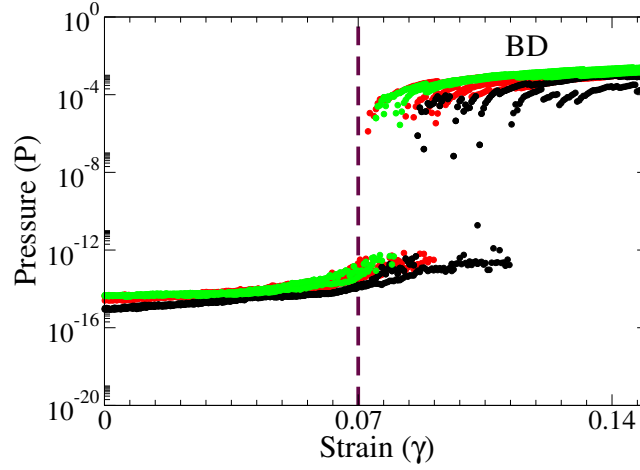


FIG. S2. **Shear jamming under uniform shear in mechanically annealed BD systems.** The pressure increases abruptly as the system is strained beyond $\gamma = \gamma_{max}$, indicating shear jamming. We present multiple realizations for each ϕ_j , where $\phi_j = 0.659$ (green), 0.656 (red), and 0.654 (black). The densities at which shear is carried out are $\phi = 0.656$ (green), 0.653 (red), and 0.650 (black).

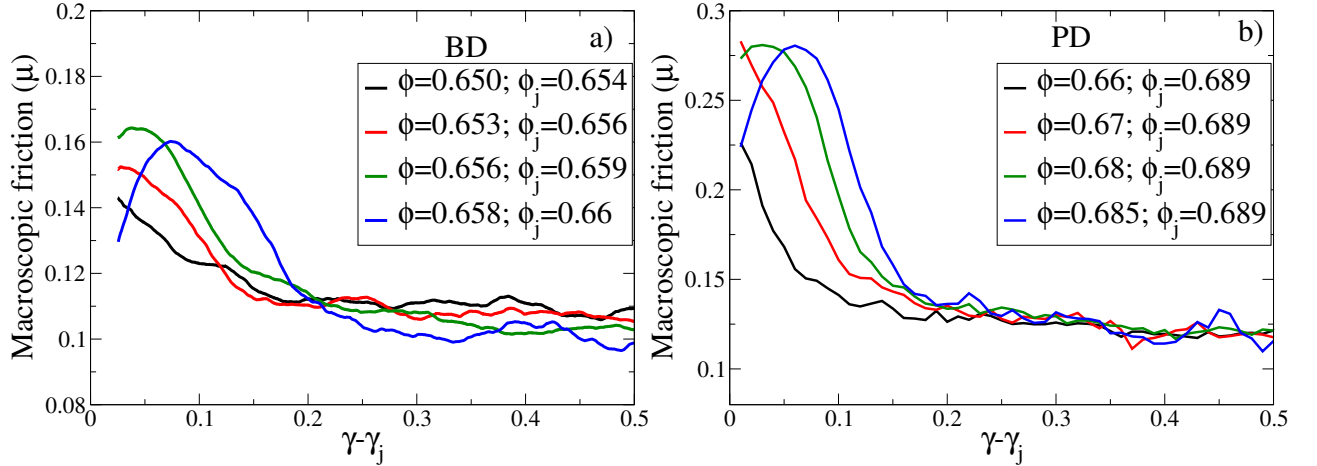


FIG. S3. **Macroscopic friction μ as a function of distance from jamming strain $\gamma - \gamma_j$ for a) BD and b) PD systems.** The jamming strain γ_j is identified as the strain at which σ_{xz} increases above 10^{-11} in BD systems, and above 10^{-8} in PD systems.

in constant volume shear simulations where the density $\phi = \phi_s$ is fixed, or the average density-strain curve $\phi(\gamma) = \langle \phi^{ind}(\gamma) \rangle$ in constant pressure shear simulations where the pressure $P = P_s$ is fixed. Here $P^{ind}(\gamma)$ and $\phi^{ind}(\gamma)$ are the pressure and density of individual samples at strain γ , and $\langle \dots \rangle$ represents the sample average. We then extrapolate the large- γ limits of $P(\gamma)$ and $\phi(\gamma)$ as the steady-state values P_s and ϕ_s . By varying the control parameter ϕ_s in constant volume shear, and P_s in constant pressure shear, we obtain the pressure EOS $P_s(\phi_s)$ for both protocols (FIG S9). The same procedure is applied to get the stress EOS $\sigma_{xz,s}(\phi_s)$.

To estimate the density ϕ_c of the critical state, we fit the EOS data $P_s(\phi_s)$ and $\sigma_{xz,s}(\phi_s)$ to the asymptotic

linear scalings near the zero pressure limit,

$$P_s(\phi_s) = P_0(\phi_s/\phi_c^P - 1), \quad (\text{A1})$$

and

$$\sigma_{xz,s}(\phi_s) = \sigma_0(\phi_s/\phi_c^\sigma - 1), \quad (\text{A2})$$

where $P_0, \sigma_0, \phi_c^P, \phi_c^\sigma$ are fitting parameters (see FIG S9). The values of the fitting parameters are summarized in TABLE S1, which show that consistently $\phi_c^P = \phi_c^\sigma$ within the numerical uncertainty. We therefore determine the critical-state density as $\phi_c = \phi_c^P = \phi_c^\sigma$.

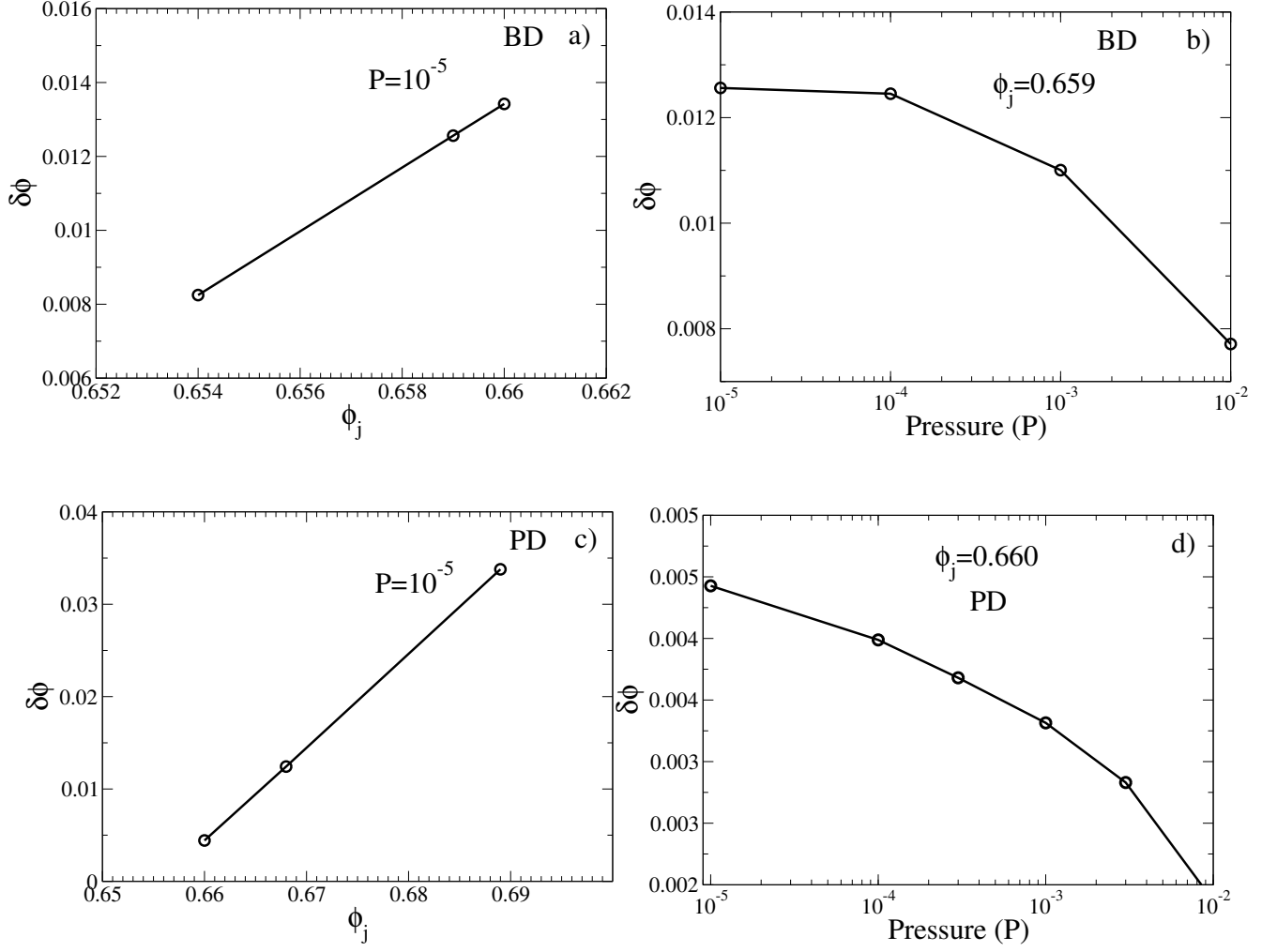


FIG. S4. **Amount of dilation in constant pressure shear deformations.** a-b) Amount of dilation $\delta\phi$ as a function of ϕ_j for a given pressure P , and c-d) as a function of P for a given ϕ_j .

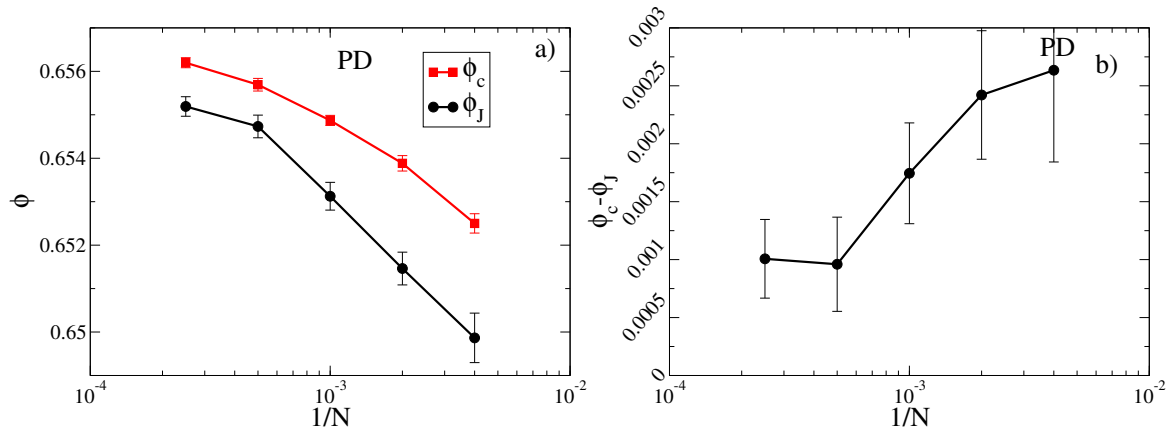


FIG. S5. **Finite size analysis of ϕ_J and ϕ_c for the PD model.** a) Densities ϕ_J and ϕ_c as functions of $1/N$. b) The difference $\phi_c - \phi_J$ is plotted as a function of $1/N$. The error bars represent standard errors.

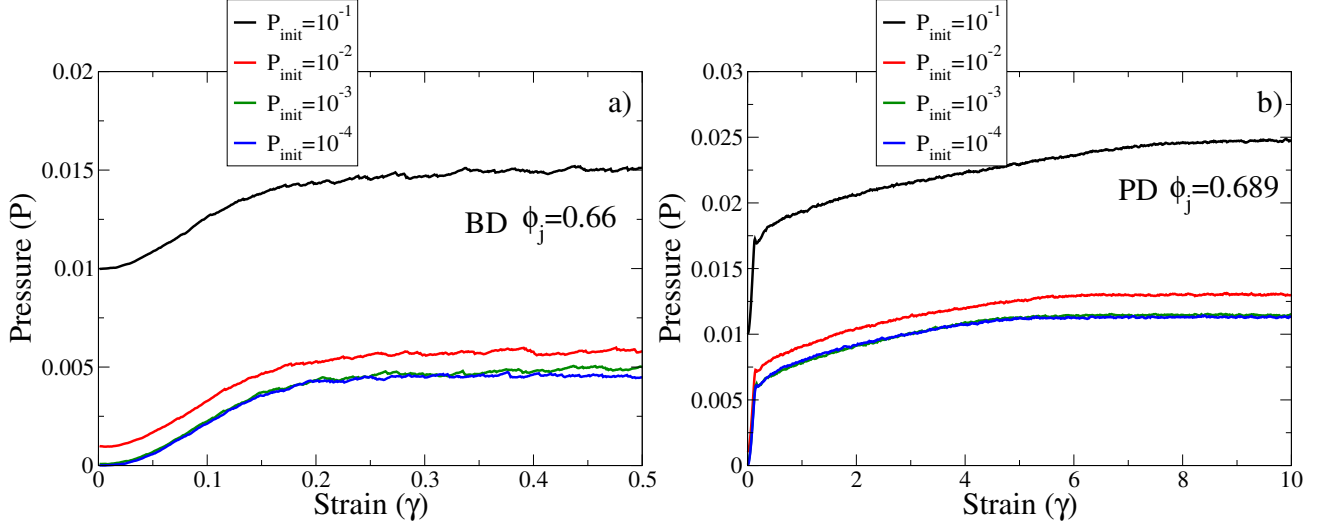


FIG. S6. **Pressure P as a function of strain γ under constant volume shear deformations, for over-compressed systems.** The pressure increases from the initial value P_{init} as the system is strained in both a) BD and b) PD systems.

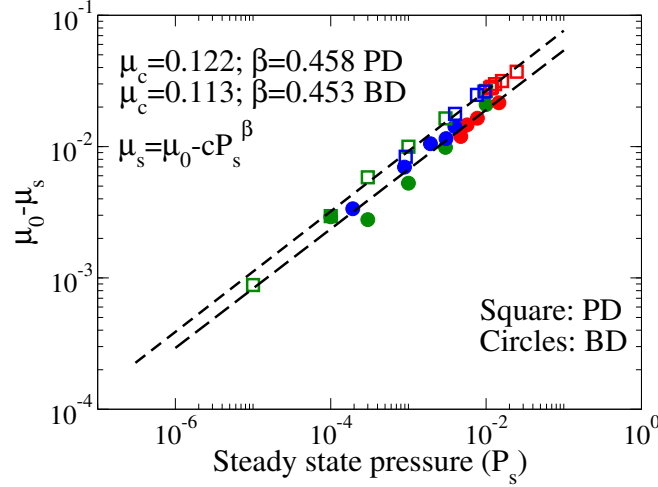


FIG. S7. **Scaling relationship between the steady-state macroscopic friction μ_s and pressure P_s .** The data for both BD ($\phi_j \approx 0.660$) and PD ($\phi_j \approx 0.689$) systems are fitted to the empirical scaling form $\mu_s = \mu_0 - cP_s^\beta$ (dashed lines). The data obtained from constant pressure shear (green), constant volume shear for $\phi_J < \phi < \phi_j$ (shear jamming, blue), and constant volume shear for $\phi > \phi_j$ (red) are presented.

b. Equation of state of isotropic-jamming

We first measure the pressure $P_{iso}^{ind}(\Delta\phi)$ at a given $\Delta\phi = \phi - \phi_J^{ind}$ for each individual sample, where ϕ_J^{ind} is the individual sample jamming density determined according to the jamming criterion described in METHODS. To do that, we compress the configuration from ϕ_J^{ind} in small increments of density $\delta\phi = 10^{-4}$, up to the target density $\phi > \phi_J^{ind}$. We then average over samples to obtain the EOS, $P_{iso}(\Delta\phi) = \langle P_{iso}^{ind}(\Delta\phi) \rangle$. The isotropic jamming density ϕ_J is determined from the average value of ϕ_J^{ind} , $\phi_J = \langle \phi_J^{ind} \rangle$. The isotropic jamming

EOS satisfies the linear scaling near ϕ_J ,

$$P_{iso}(\phi) = P'_0(\phi/\phi_J - 1), \quad (\text{A3})$$

where $P'_0 = 0.29$ (BD model) and 0.21 (PD model) are used to re-scale P_{iso} such that the isotropic jamming and the steady-state EOSs collapse onto the universal curve (Fig. 3a). The values of ϕ_J and P' are listed in TABLE S1.

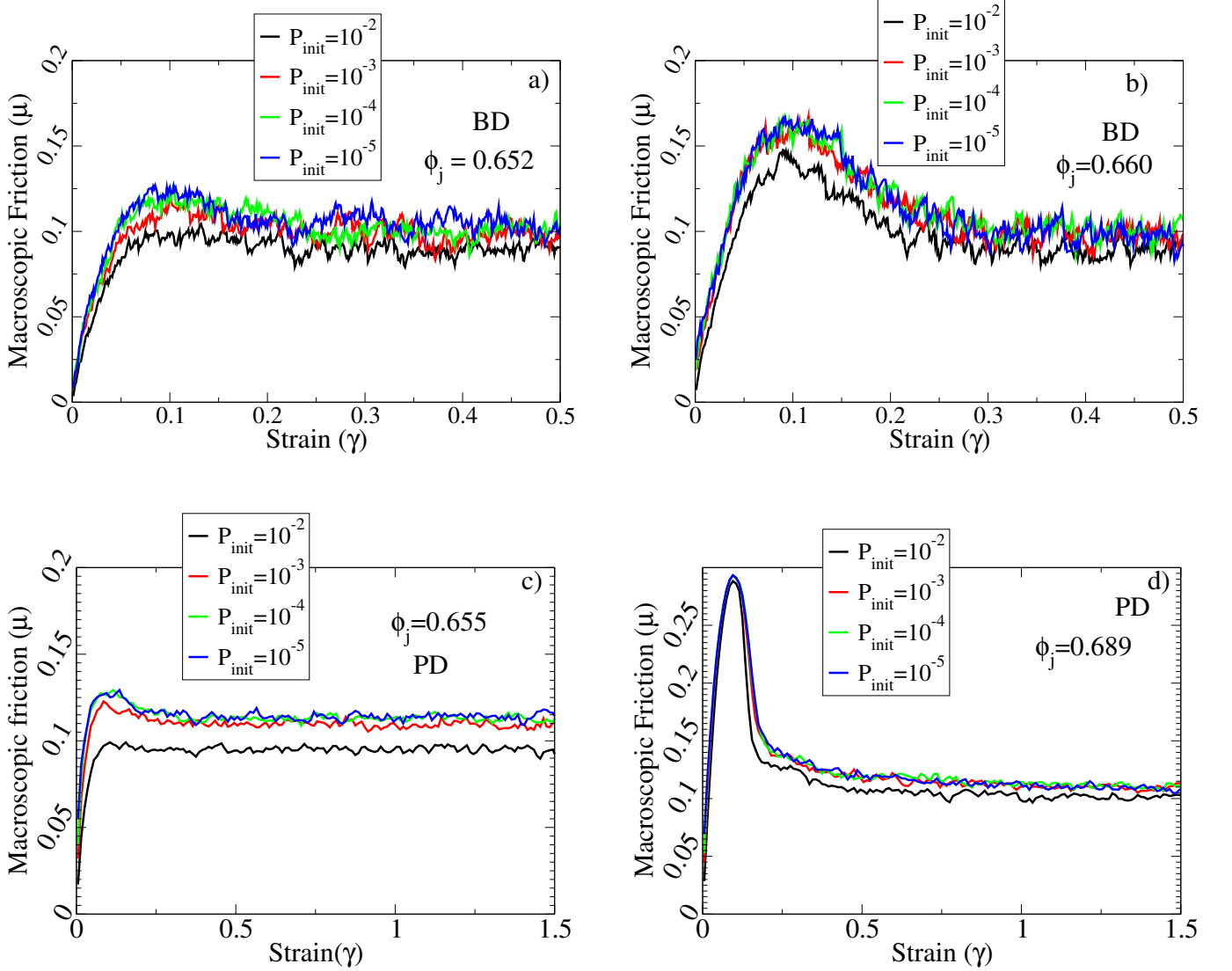


FIG. S8. **Microscopic friction μ of over-compressed systems ($P_{init} > 0$, $\phi > \phi_j$) as a function of strain γ under constant volume shear.** Data are plotted for two different ϕ_j and four different P_{init} in both BD and PD models.

	P_0	ϕ_c^P	σ_0	ϕ_c^σ	P'_0	ϕ_J
BD	0.261	0.647	0.024	0.647	0.29	0.648
PD	0.217	0.656	0.021	0.656	0.21	0.655

TABLE S1. Values of fitting parameters in Eqs. (A1), (A2), and (A3), for both BD ($\phi_j = 0.660$) and PD ($\phi_j = 0.689$) models. The steady-state data, P_0 , ϕ_c^P , σ_0 and ϕ_c^σ , are obtained from constant pressure shear; the constant volume shear gives the same results because the EOSs are independent of shear protocols (see FIG S9).

6. Additional data for the generalized zero-temperature jamming phase diagram

In FIG S10 we show the generalized zero-temperature jamming phase diagram for the BD model. Similar to the PD case (Fig. 4), the yield stress shows a discontinuous jump at ϕ_j for $\phi_j > \phi_J$. This behavior is independent of

the definition of the yield stress, which can be seen from Fig. 4 where σ_Y is defined as the steady-state value σ_s , and from FIG S11 where σ'_Y is defined as the peak value of the shear stress in the stress-strain curve (both figures are for the PD model).

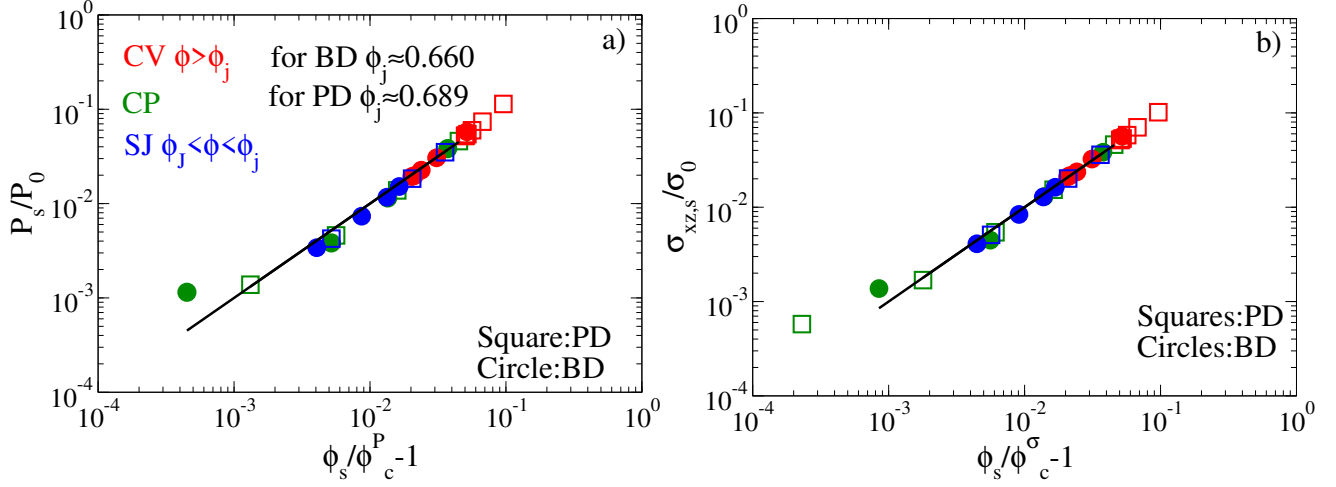


FIG. S9. **Critical scalings of steady-states.** We fit the EOS data of (a) pressure and (b) stress to Eqs. (A1) and (A2). The fittings are represented by solid lines.

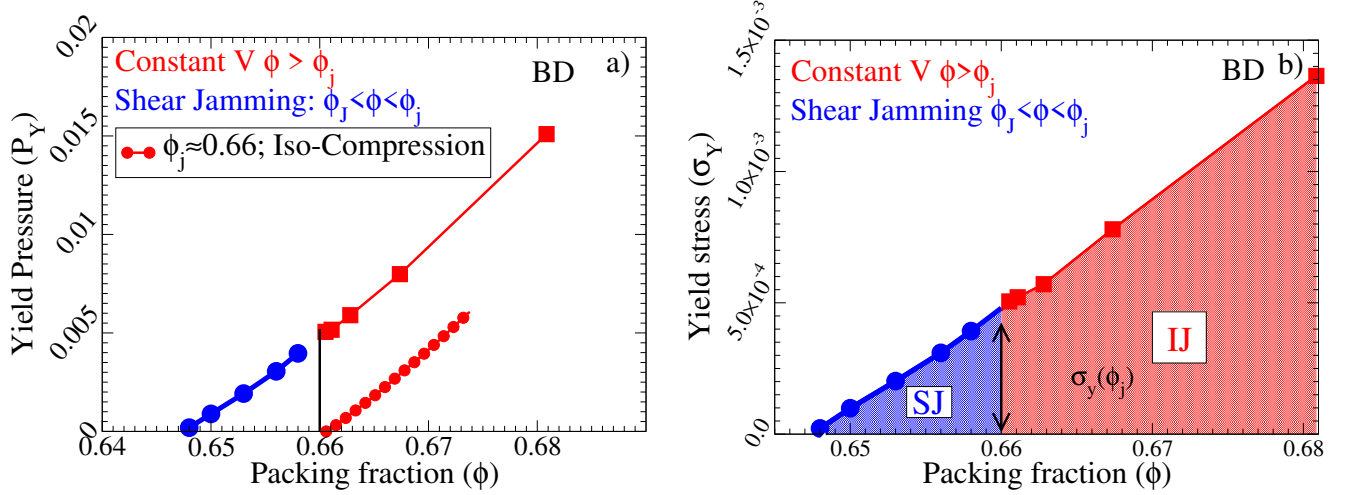


FIG. S10. **Generalized zero-temperature jamming phase diagram for the BD model.** **a)** Yield pressure ($P_Y = P_s$) as a function of packing density ϕ , obtained by constant volume shear deformations for both $\phi > \phi_j = 0.66$ (isotropic jamming, IJ) and $\phi < \phi_j$ (shear jamming, SJ). The isotropic compression pressure P_{iso} is also plotted. **b)** Yield stress ($\sigma_Y = \sigma_{xz,s}$) as a function of ϕ .

7. Jamming densities of mechanically annealed bi-disperse sphere packings

An over-jammed BD system at packing density ϕ (compressed from $\phi_J \simeq 0.647$), unjams under constant volume cyclic AQS, and jams again at ϕ_j ($\phi_j > \phi > \phi_J$) upon a further compression. The jamming density ϕ_j depends

on both the unjamming density ϕ and the strain amplitude γ_{max} of the cyclic shear. As shown in the FIG S12, ϕ_j increases with γ_{max} for a fixed ϕ , and increases with ϕ for a fixed γ_{max} . In the main text, we use $\gamma_{max} = 0.07$, because for this amplitude, the largest range of densities over which unjamming occurs is obtained [31].

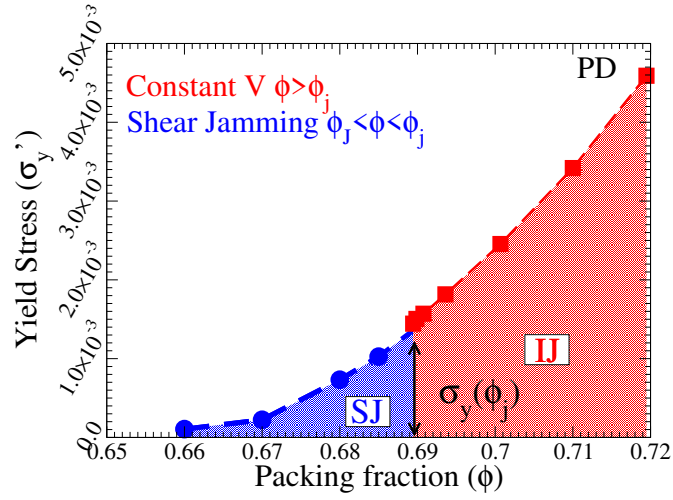


FIG. S11. Generalized zero-temperature jamming phase diagram for the PD model, where the yield stress σ'_Y is defined as the peak value of the shear stress in the stress-strain curve. The jamming density is $\phi_j = 0.69$.

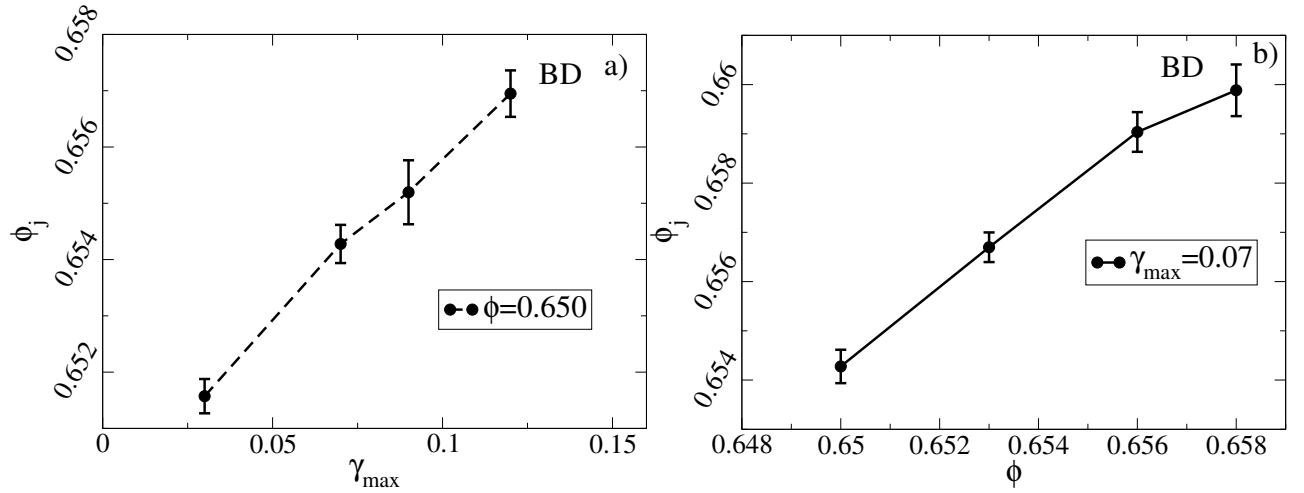


FIG. S12. Dependence of jamming density ϕ_j on protocol parameters of cyclic AQS, for the BD model. a) Dependence of jamming density ϕ_j on the strain amplitude γ_{max} , for a fixed unjamming density $\phi = 0.650$. b) Dependence of jamming density ϕ_j on the unjamming density ϕ , for a fixed $\gamma_{max} = 0.07$. Error bars represent standard deviations.